Journal of Thermal Analysis and Calorimetry
https://doi.org/10.1007/s10973-025-14182-z

Unveiling the nucleation and growth kinetics of mullite crystals in kaolin and natural phosphate compounds

Fateh Chouia[1,2] · Hocine Belhouchet[3] · Toufik Sahraoui[4] · Yousf Islem Bourezg[5,6] · Mohamed Hamidouche[7] · Anne Leriche[8]

Received: 24 July 2024 / Accepted: 4 March 2025

Abstract
The nucleation and growth kinetics of mullite crystal structure prepared from Algerian natural phosphate (NP) and kaolin materials were studied by differential thermal analysis (DTA) and X-ray diffraction (XRD). The XRD patterns showed that mullite, hydroxyapatite and anorthite were the main crystal structures present in mixtures. From DTA results, several thermal characteristics including the crystallization peak temperature, activation energies, were calculated. The DTA results showed that the characteristics temperature and activation energies were reduced when the NP content was increased at the expense of kaolin material. Bulk crystallization was seen in samples with low/moderate and high NP amounts, respectively, with a fixed ($n = m = 3$) and growing ($n = 3$ and $m = 3$) number of nuclei. As a result, it is possible to produce the mullite phase using Algerian kaolin raw material and natural phosphate that can be added as a structural modifier of the growth process.

Keywords Natural phosphate · Kaolin · Compounds · Mullite crystal structure · Thermal analysis

Introduction

Mullite ($3Al_2O_3{\cdot}2SiO_2$) crystal structure is a valuable material in the industry with regard to its exceptional mechanical strength, resistance to thermal shock, and thermal stability, made it as a potential material for ceramics used in advanced applications like electronic packaging, catalyst supports, optical devices, filters, and heat exchangers [1–4]. Mullite is generally synthesized using several methods, such as sintering [5], sol–gel [6], co-precipitation [7], hydrothermal [8], flash combustion [9], and chemical vapor deposition [10]. In order to reduce the cost of the preparation of mullite material, many studies have been carried out to synthesize mullite from mineral raw materials such as kyanite [3], coal fly ash [11], kaolin [12], bauxite [13] and halloysite [14]. However, due to its low cost and relatively low sintering temperature, kaolin has been explored in recent decades for use in conventional ceramics, and there has been increased interest in turning kaolin into mullite [15]. Moreover, beyond 1273 K, kaolinite phase transforms during the removal of water and hydroxyl groups directly into mullite with a vitreous phase [16].The morphology of the generated mullite is bimodal (i.e. primary and secondary). In addition, the primary mullite made by the slow collapse of metakaolin at 1263 K, has an extended crystal structure. In contrast, the secondary mullite with an acicular grain structure is created when the glass phase is solution-precipitated with alumina particles present [3].

It is feasible to swiftly and precisely record the thermal changes that take place when a specimen is heated through

✉ Hocine Belhouchet
hocine.belhouchet@univ-msila.dz

1 Laboratory of Thin Film Physics and Applications, University of Biskra, BP. 145 RP, 07000 Biskra, Algeria

2 Department of Mechanical Engineering, University of Biskra, BP. 145 RP, 07000 Biskra, Algeria

3 Physics Department, Faculty of Sciences, University Pole, Road Bourdj Bou Arreiridj, 28000 M'sila, Algeria

4 Higher Normal School, 28001 Boussaada, M'sila, Algeria

5 Faculty of Technology, University of M'sila, University Pole, Road Bourdj Bou Arreiridj, 28000 M'sila, Algeria

6 Physico-Chemistry of Materials and Environment Laboratory, Ziane Achour University of Djelfa, BP 3117, Djelfa, Algeria

7 Emerging Materials Research Unit, Ferhat Abbass University of Setif 1, Campus El Bez, 19000 Setif, Algeria

8 CERAMATHS – Laboratoire de Matériaux Céramiques Et de Mathématiques, Université Polytechnique Hauts-de-France, INSA Hauts-de-France, 59313 Valenciennes, France

Published online: 21 April 2025

the analysis method known as differential thermal analysis (DTA) [17]. This approach was also utilized to explore crystallization kinetics in ceramics, calculate homogenous crystal nucleation rates, and derive the activation energy for new phase crystallization [18]. Several studies have investigated the kinetics of mullite generation from various materials, including kaolin ceramics [19], aluminum silicate glass fiber [20], diphasic gels [21], porcelain stoneware [22] and combination of raw wastes with a high amount of silica and aluminum hydroxides [23]. Furthermore, the mullitization process is highly dependent on experimental factors such as the order of the kaolinite structure [19], impurities, heating rate, pressure, particle size distribution, particle shape, surface morphology, and other structural characteristics [24]. The process of mullite formation from pure alumina and Algerian kaolin have been investigated; Sahnoune et al. [19] have assessed the growth morphological parameters, activation energies, and formation temperature. By using the Kissinger technique and the isothermal method, the activation energies of mullite crystallization were determined to be 1260 and 1290 kJ mol^{-1}, respectively. It was found that the growth characteristics n and m were nearly equivalent to 1.5. The activation energies for crystallizing monolithic mullite synthesized from Algerian kaolin was 577.92 kJ mol^{-1} [2]. In addition, the growth characteristics parameters n and m were ~ 1.5. The first investigation on the mullite crystallization kinetics of monophasic precursors, with activation energy values of 293 and 362 kJ mol^{-1} was studied by Li and Thompson [25]. These values were eventually shown to be significantly lower than those given by other authors. Nucleation was the regulating stage for mullitization from the monophasic gel, according to Li and Thompson [25]. The synthesis of both primary and secondary mullite from wastes rich in silica and alumina required activation energies of 431 and 454 kJ mol^{-1}, respectively [26].

Few data about the effect of natural phosphate or CaO powders on the crystallization kinetics of mullite phase can be found in the literature. Pooladvand et al. [27] studied the effect of CaO and MgO on the transformation of andalusite. The authors have concluded that the MgO and CaO lowered the mullite production temperature by at least 373 K. Qiankun et al. [28] studied the effect of CaO impurity on the crystallization of mullite from SiO_2 gel and Al_2O_3 powders. They concluded that in the oxidizing atmosphere, the introduction of CaO can enhance the formation of mullite and reduces the temperature of liquid formation.

According to the authors, no research has addressed the thermodynamic properties of mullite crystallization from Algerian natural phosphate (NP) and kaolin materials. In earlier study [29], we studied extensively the reaction sintering in seven pairs of natural phosphate (NP) and kaolin (DD2) local substances.

Thus, using differential thermal analysis (DTA), the kinetics of the mullite phase formation was investigated by reacting sintering of Algerian kaolin containing natural phosphate substance at non-isothermal conditions. A number of thermodynamic parameters were measured, including the morphological parameters n and m, peak temperature T_c, enthalpy $\Delta H^{\#}$, activation energy E, Gibbs free energy $\Delta G^{\#}$, enthalpy $\Delta H^{\#}$, entropy $\Delta S^{\#}$, and others.

Experimental procedure

In this study, kaolinite and natural phosphate powders from the north-east of Algerian country, Djabal Debagh region and the mine of Djebel El-Onk, were used in this investigation, resepectively. The particles size of kaolin and natural phosphate materials were ~ 0.37 µm and ~ 0.64 mm, respectively. More details about the initial microstructures of the powders were reported in our earlier work [29]. A homogenous mixture of kaolin and natural phosphate was prepared using the ball milling process for 5 h. After drying at 383 K, the slurry was ground into a powder and sieved using a 63 µm mesh screen. Three compositions were created by altering the proportion of natural phosphate from 30 to 70 mass% (are labelled 30NP, 50NP and 70NP). These mixtures were studied extensively in our previous work [30] by BET method, XRD analyses, FT-IR spectroscopy, linear thermal expansion, bulk density, open porosity, and scanning electron microscopy.

For the DTA experiment, samples weighing about 40 mg were heated at various heating rates (5, 10, 20, and 30 °C min^{-1}) from room temperature to 1500 K in an alumina crucible. The measurements were conducted in air using Setaram Setsys 16/18 simultaneous TG/DTA analyser.

X-ray diffraction (XRD) patterns were obtained using the Bruker D8 diffractometer, functioning at 35 kV and 30 mA. Cu-Kα radiation was used in the analysis, and the step size was set at 0.05° and the scanning speed was 37°/min. The three compounds mentioned above were all subjected to XRD testing after being heat-treated for two hours at 1473 K under standard conditions.

A scanning electron microscopy, SEM (Model, Hitachi S3500-N) operating at an accelerating voltage of 20 kV, was used to examine the morphology and microstructure.

Results and discussion

DTA thermal scans of all samples at four distinct speeds of heating (β) are shown in Fig. 1. The DTA results show three endothermic peaks E_1, E_2, and E_3 and three other ones with an exothermic trend P_1, P_2 and P_3, as shown in Fig. 1a–d.

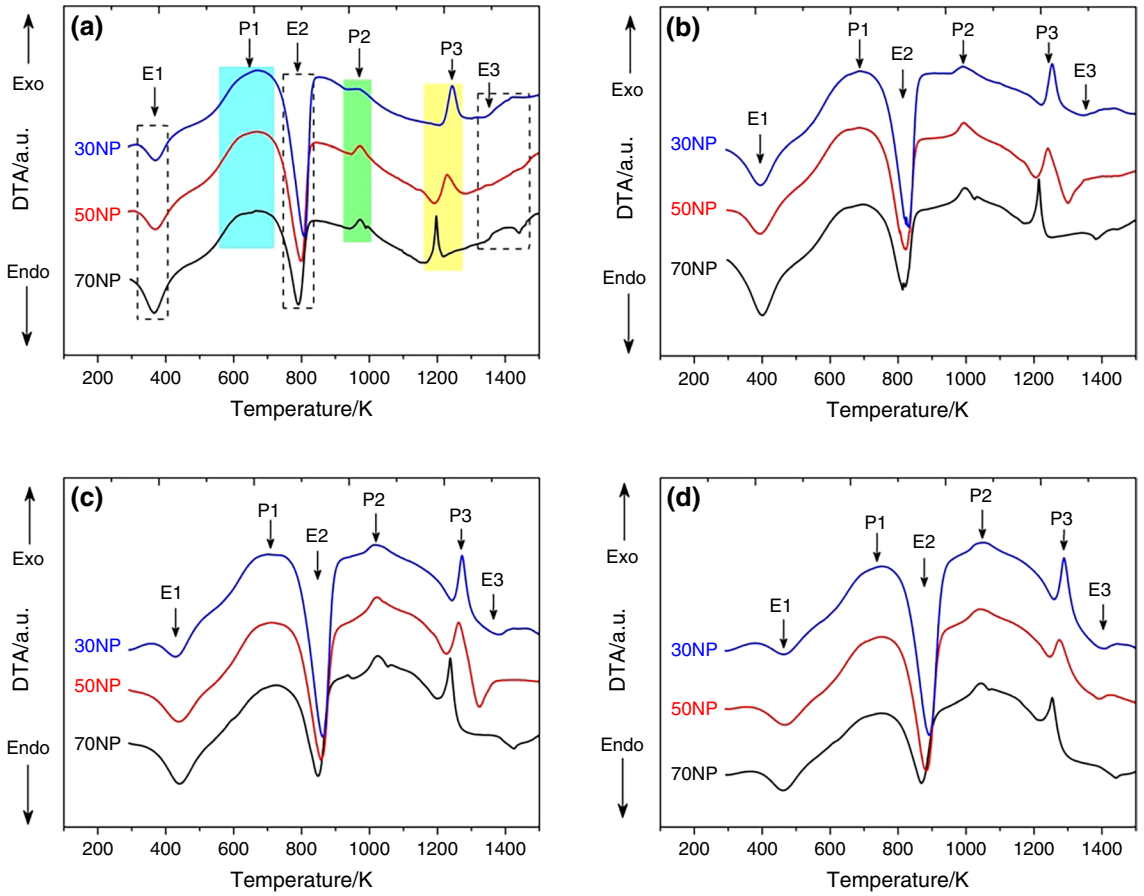

Fig. 1 Plots of DTA scan results of 30NP, 50NP, and 70NP compounds at different heating rates, **a** 5, **b** 10, **c** 20, **d** 30 K min^{-1}

The first endothermic peak E_1 in the temperature range of 200–400 K is caused by the departure of the surface water [31]. The second endothermic peak E_2, which is detectable in the temperature range of 750 to 900 K, is associated with the dihydroxylation of kaolinite and then the production of metakaolinite [32]. The DTA curves present other endothermic effects above E_3 with low intensities, which can be detected in the range of 1300–1400 K and are corresponded to the decomposition of hydroxyapatite phase [33].

The exothermic peak P_1, observed around of 700 K, is due to the burning of organic materials from natural phosphate [34]. The peaks P_2 and P_3 with exothermic behaviour appeared around 900–1000 K and 1200–1300 K, respectively. The partial crystallization of hydroxyapatite is recognized by the exothermic peak P_2 around 900–1000 K [35], while the peak P_3 which appear from 1200 to 1300 K, corresponds to the formation of the primary mullite from metakaolin [36]. The variation in mullite formation temperatures in different studies may be attributed to the difference in particle size distributions and chemical compositions of the kaolin material [19]. Gao et al. [37] investigated how the microstructure, sintering temperature, and mechanical characteristics of mullite were affected by the initial kaolin powder particle size. They reported that when the particle size was decreased from 48 to 38 µm, the mullitization temperature allowed a reduction of 373 K. F. Rouabhia et al. [38] reported that the transformation of metakaolinite to mullite phase occurred from kaolin and different proportions of calcite and carbonate materials with a particle size of 50 µm, was ranged from 1137 to 1268 K [38]. The temperature at which primary mullite was formed in this work is comparable to that to be obtained at about 1263 K by sintering of kaolin and alumina mixtures with the same starting particle size of 63 µm [39].

The temperature at which primary mullite was formed in this work is comparable to that to be obtained at about 1263 K by sintering of kaolin and alumina mixtures with the same starting particle size of 63 µm.

In this investigation, the following reactions can be used to illustrate the transition from the kaolinite to the mullite phase [40–42]:

$$Al_2O_3.2SiO_2.2H_2O(\text{kaolinite}) \overset{673\sim773K}{\rightarrow} Al_2O_3.2SiO_2(\text{metakaolinite}) + 2H_2O \quad (1)$$

$$2(Al_2O_3.2SiO_2) \overset{\sim 1253K}{\rightarrow} Si_3Al_4O_{12}(Al-Si-\text{spinel}) + SiO_2(\text{amourphous}) \quad (2)$$

$$Si_3Al_4O_{12} \overset{>1273K}{\rightarrow} 2(3Al_2O_3.2SiO_2)(\text{mullite}) + 5SiO_2(\text{amourphous}) \quad (3)$$

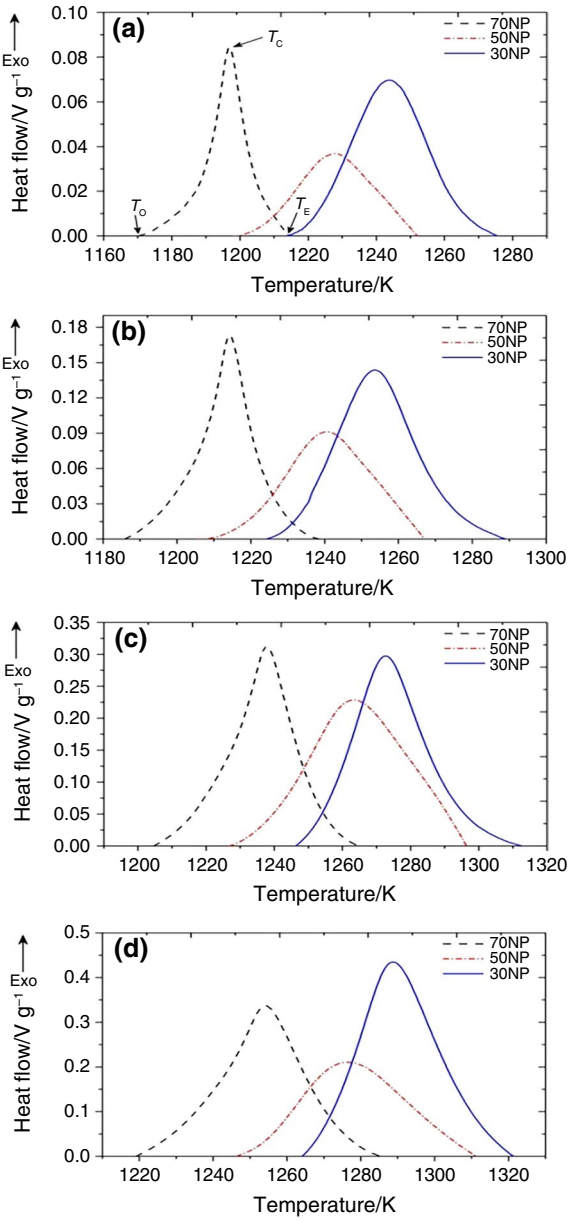

Fig. 2 Normalized mullite crystallizationpeaks of different compounds at different heating rates: **a** 5, **b** 10, **c** 20, **d** 30 K min^{-1}

Effects of NP and heating rate on the characteristics temperature and x conversion

Figure 2 reveals the normalized mullite crystallization peaks of different mixtures with different heating rates. The temperature of crystallization values, T_c, which corresponds to the top of the curve, are presented in Fig. 3. It is clear that T_c values shift to a higher temperature of 1290.6 K as the amount of phosphate decreases to 30% and the heating rate increases to 30 K min^{-1}. Obviously, the shift of the start of crystallization towards lower temperatures is really caused by a greater number of nuclei since they take longer to nucleate at lower heating rates.

Therefore, due to the fact that crystallization takes place more rapidly when subjected to higher heating rates, the resulting peak becomes narrower and exhibits greater intensity compared to peaks generated under slower heating rates, as depicted in Fig. 2a–d [43].

The x conversion can be easily calculated from the DTA results using the following expression [44, 45]:

$$x = \frac{A_T}{A} \quad (4)$$

where A_T is the area between the onset peak and the selected temperature T, and A is the entire area of the exothermic peak.

Figure 4 shows the variation of the x conversion of mullite formation for different compounds against the heating temperature under different heating rates 5 (Fig. 4a), 10 (Fig. 4b), 20 (Fig. 4c), and 30 K min^{-1} (Fig. 4d). From these figures, the plots of x for each compound shift toward high values of T with the heating rate increasing, which confirms that the crystallization process of mullite is kinetically managed and thermally activated. Moreover, this finding

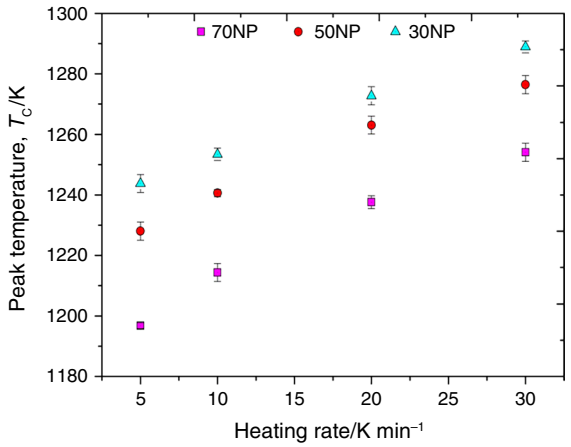

Fig. 3 Mullite crystallizationpeak temperatures for 30NP, 50NP, and 70NP compounds at different heating rates up to 30 Kmin^{-1}

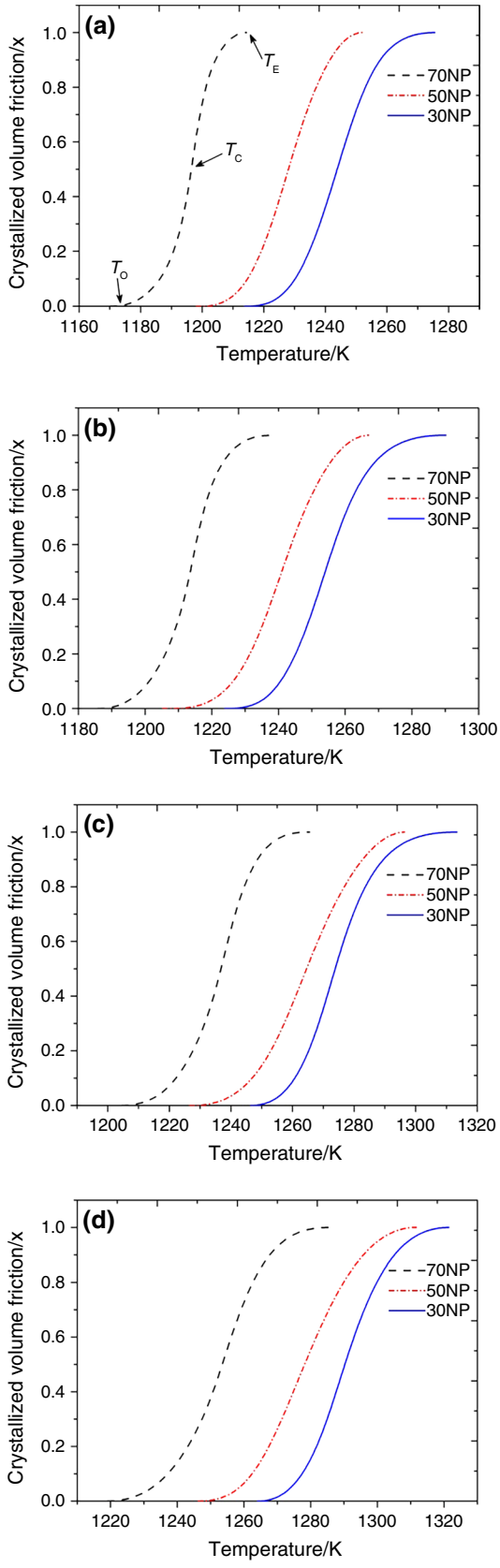

Fig. 4 Crystallized volume fraction X of different samplesat different heating rates: **a** 5, **b** 10, **c** 20, **d** 30 K min^{-1}

confirms the variation of formation rate dx/dt of the mullite phase vs. time for the 50 NP sample (Fig. 5a), where it increases with heating rate increasing to achieve 0.0148 s^{-1} with a lower formation time ~ 134 s at 30 K min^{-1}. In addition, from Figs. 4–5b, it is clear that the phosphate content had a significant role in the mullite growth characteristics by lowering and increasing the crystallization temperature and formation rate, respectively. The more natural phosphate added, the lower mullite crystallization temperature. Moreover, the difference in the formation rate for the 70 NP sample (i.e. ~ 0.009 s^{-1}) and the remaining samples (i.e. ~ 0.006 s^{-1}) may be attributed to the change in the growth mechanism. This behaviour can be linked to the CaO amount that is raised after calcite decomposition above 1028 K and comes from natural phosphate itself, which acts as a fluxing agent, reducing the difference between the beginning and ending of mullite crystallization temperature [46], as well as other phenomena such as hydroxyapatite [34] and sintering processes [47].

Activation energies and thermodynamic parameters

The activation energy of the crystallization phenomenon E_{KAS} at different values of x can be determined by using the Kissinger–Akahira–Sunose (KAS) approach as follows [48, 49]:

$$\ln\left(\frac{\varnothing_i}{T_{x,i}}\right) = -\frac{E_{KAS}}{RT_{x,i}} + C_K(x) \tag{5}$$

where $T_{x,i}$ is the crystallization temperature at heating rate $\varnothing_i$ and crystallized fraction x and $C_K(x)$ is a constant with relation to x.

The plots of $\ln(\varnothing_i/T^2_{X,i})$ versus $10^3/T_{X,i}$ corresponding to the mullite formation for 30 NP, 50 NP, and 70NP compound samples are shown in Fig. 6a–c, respectively. The plots exhibit linear behaviour, and the deduced activation energies from the slopes of the plots, are presented in Table 2 and in Fig. 6d. It is obvious that the local energy for all samples decreases with the growth of mullite crystal structure. This trend confirms that the energy needed to initiate the nucleation process to occur is quite large, continually decrease sup on the growth stage [45]. On the other hand, the decrease in phosphate content favours the increase in crystallization activation energy to reach a value of 557.03 kJ mol^{-1} in the 30NP sample at 10% of x, whereas the lower value 335.13 kJ mol^{-1} is observed in 70NP at 90%.

The thermodynamic parameter of local activated enthalpy $\Delta H^{\#}$ was calculated at different heating rates using the following equation [40, 50]:

$$\Delta H^{\#}_i = E_{a,i} - RT_i \tag{6}$$

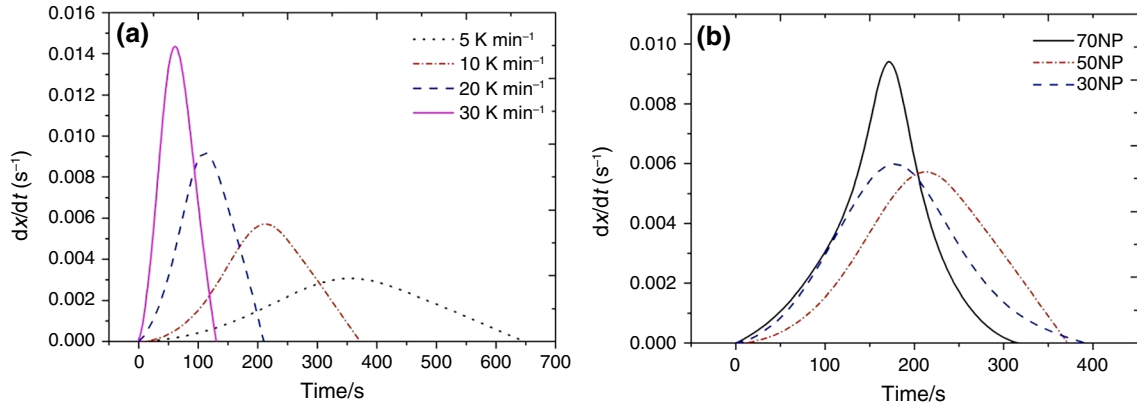

Fig. 5 Heating rate dx/dt curves vs. time of the 50NP sample at different heating rates **a** and for different compounds at a fixed heating rate of 10 K min^{-1}

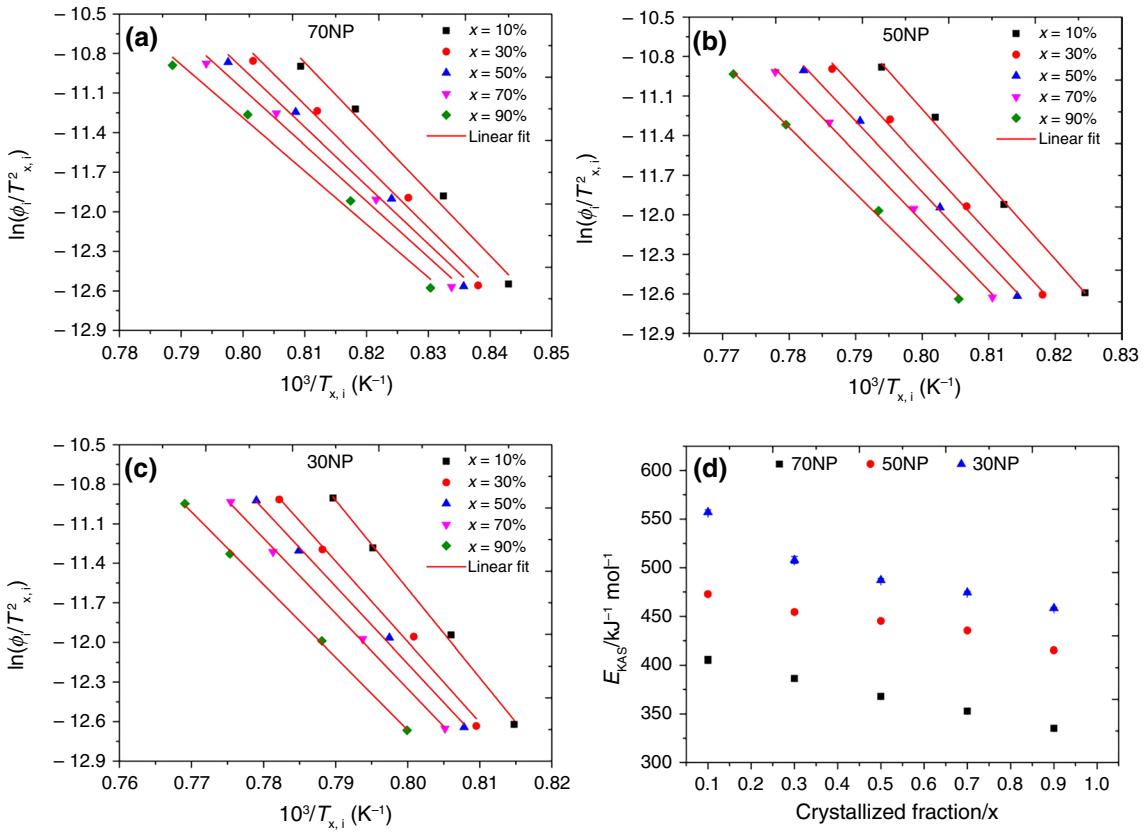

Fig. 6 Plots of, **a–c** $\ln(\varphi_i/T^2_{x,i})$ against $1000/T_{x,i}$ of different compounds; **d** E_{KAS} for different samples vs. crystallized fraction

where $E_{a,i}$ is local activation energy that corresponds to E_{KAS} at heating rate i.

The obtained values of local enthalpy $\Delta H_i^{\#}$ as well as its average value are shown in Table 1. The average values of $\Delta H_i^{\#}$ are in the range of 447.69–546.60, 404.65–462.51 and 324.85–395.32 kJ mol^{-1} for 30NP, 50NP, and 70NP, respectively. It is clear that the local enthalpy energy varies as the same as the E_{KAS}, where it decreases with the increase of both x value and phosphate content.

Table 1 Crystallization energies characteristics E_{KAS} and $\Delta H^{\#}$for different glasses at different x and β values

Sample	x \%	E_{KAS}\kJ mol^{-1}	$\Delta H_i^{\#}$\kJ mol^{-1}				
			5	10	20	30	Average of $\Delta H_i^{\#}$\kJ mol^{-1}
			β\K min^{-1}				
30NP	10	557.03 ± 2.4	546.80	546.71	546.54	546.40	546.60 ± 2.4
	30	507.98 ± 3.62	497.68	497.59	497.43	497.72	497.49 ± 3.62
	50	487.2 ± 1.88	476.85	476.77	476.60	476.47	476.66 ± 1.88
	70	474.47 ± 1.21	464.07	463.99	463.82	463.69	463.88 ± 1.21
	90	458.35 ± 0.98	447.89	447.80	447.62	447.49	447.69 ± 0.98
50NP	10	472.81 ± 1.93	462.72	462.61	462.44	462.31	462.51 ± 1.93
	30	454.52 ± 2.22	444.35	444.25	444.06	443.94	444.15 ± 2.22
	50	445.21 ± 1.8	435.00	434.89	434.69	434.58	434.79 ± 1.8
	70	435.40 ± 1.33	425.14	425.02	424.82	424.71	424.92 ± 1.33
	90	415.20 ± 1.41	404.87	404.76	404.53	404.42	404.65 ± 1.41
70NP	10	405.55 ± 3.66	395.68	395.56	395.38	394.96	395.32 ± 3.66
	30	386.43 ± 3.15	376.50	376.37	376.19	376.05	376.28 ± 3.15
	50	368.00 ± 3.13	358.05	357.91	357.71	357.57	357.81 ± 3.13
	70	352.76 ± 2.95	342.78	342.63	342.43	342.28	342.53 ± 2.95
	90	335.13 ± 2.87	325.11	324.95	324.74	324.58	324.85 ± 2.87

Figure 7 illustrates the curves of Kissinger method [49], Augis–Bennett model (1) [51] and Augis–Bennett model (2) [52], given by the Eqs. (7–9), respectively:

$$\ln\frac{T_c^2}{\beta} = \frac{E_{ck}}{RT_c} + \text{constant} \tag{7}$$

$$\ln\frac{\beta}{(T_c - T_0)} = -\frac{E_{cab1}}{RT_c} + \ln(k_0) \tag{8}$$

$$\ln\frac{T_c}{\beta} = \frac{E_{cab2}}{RT_c} - \ln(\nu) \tag{9}$$

where E_{ck}, E_{cab1} and E_{cab2} are the energies of activation highlighted using the Kissinger and Augis-Bennett models(1) and (2), respectively;ν is the number of endeavors performed by the nuclei per second to break the energy barrier for crystallization; k_0 is the frequency or pre-exponential factor; and T_0 is the initial DTA scan temperature.

The plots in Fig. 7give straight lines, where the activation energies should be calculated from their slopes. The obtained values are shown in Table 2 and Fig. 7d. The E_{cab1} values are close to those obtained from E_{cab2}, where both methods give slightly higher values than the E_{ck} one. Notably, E_{ck} energies closely approach those obtained using the Kissinger–Akahira–Sunose (KAS) technique, with x values ranging around 50% for mullite cristallization. In contrast, the E_{cab1} and E_{cab2} values are somewhat higher than those shown in Table 1.

Many authors [53, 54] reported the activation energy for mullite formation. Ondro et al. [53] found the activation energy of 726 kJ mol^{-1} for mullite production from kaolinite. Elmas et al. [54] used differential thermal analysis (DTA) to examine the non-isothermal kinetics of mullite crystallization in a mechanically activated kaolinite–alumina ceramic system; they reported the activation energy values for crystal growth step between 913 and 495 kJ mol^{-1}. As noted in the literature, variations in the chemical composition of raw materials lead to distinct energies of activation and reaction processes, with certain metal oxides (nucleating agents, stabilizers, and fluxes) generally influencing various variables and stages of nucleation and crystallization [2, 55].

The k_0 parameter can be estimated using the Eq. (8). The obtained values are 5.60×10^{18}, 1.27×10^{17} and1.39×10^{14} s^{-1}for 30NP, 50NP, and 70NP mixtures, respectively.

According to Eq. 9, the values of ν parameter can also be calculated from Fig. 7 plots and are shown in Table 2.The trends of ν can be used to determine accessible nucleation sites for crystal development. The obtaining values of ν are 5.83×10^{18}, 1.33×10^{17}, and 1.45×10^{14} s^{-1}for 30NP, 50NP, and 70 NP, respectively. We note that the values of ν parameter increase with the decrease of phosphate in mixtures. This suggests that nuclei make the most tries per second to cross the energy barrier, whereas the lower CaO content hinders this behavior, and thereby increasing the activation energies. Furthermore, the transformed structural units may be non-uniform, and other competing processes intervene, such as the degree of depolymerization, hence elevating activation energy. A second explanation could be that Si–O

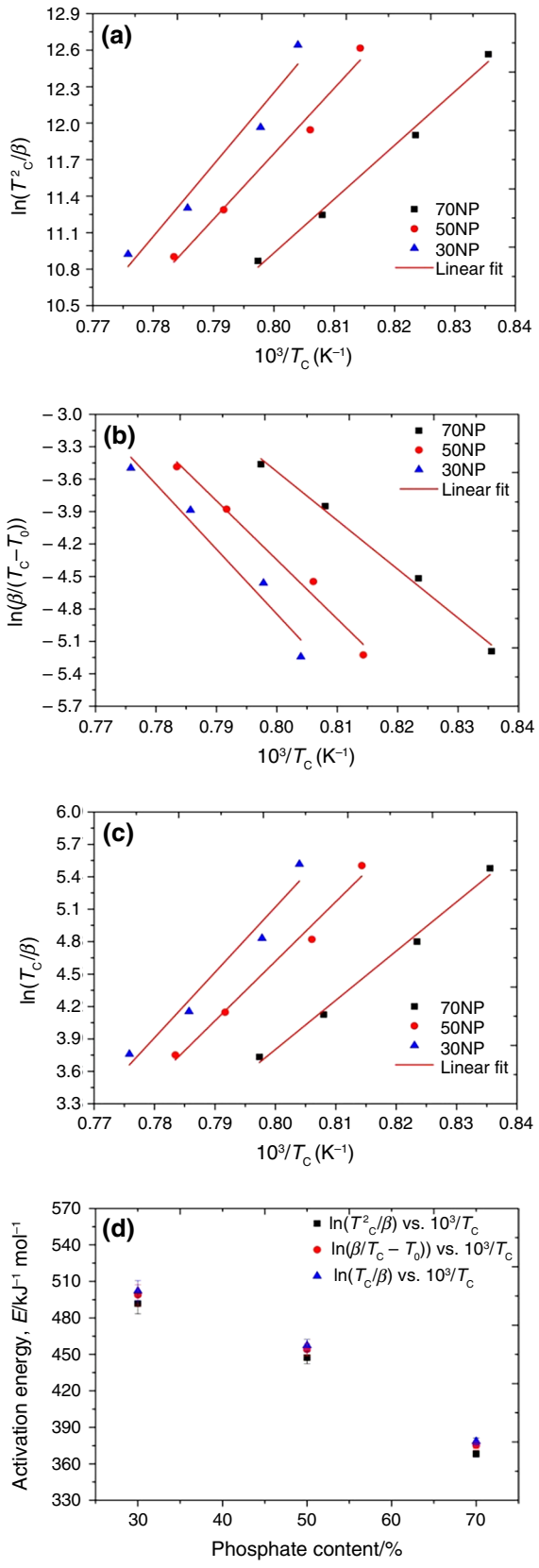

Fig. 7 Plots of, **a** $\ln(T_C^2/\beta)$, **b** $\ln(\beta/(T_C - T_0))$, **c** $\ln(T_C/\beta)$, vs. $10^3/T_C$, and **d** Values of activation energy using different methods with different phosphate ratio

and Al–O have larger bonding energies than Ca–O, leading to a higher thermodynamic barrier to mullite crystallization, which involves rearranging the short- to medium-range structure [20].

The thermodynamic parameters including enthalpy ($\Delta H^{\#}$) and Gibbs free energy ($\Delta G^{\#}$) as well as entropy ($\Delta S^{\#}$) of the process, were highlighted using the following equations [50, 56]:

$$k_0 \exp\left(\frac{-E}{RT}\right) = \xi \exp\left(\frac{-\Delta G^{\#}}{RT}\right) \tag{10}$$

$$\Delta G^{\#} = \Delta H^{\#} - T\Delta S^{\#} \tag{11}$$

where $\xi = kT/h$, k and h are the Boltzman and Plank constants, respectively.

From Table 2, it is obvious that Gibbs free energy $\Delta G^{\#}$ and the enthalpy $\Delta H^{\#}$ for mullite phase have positive values, while the entropy $\Delta S^{\#}$ has negative values. The average values of $\Delta H^{\#}$, $\Delta G^{\#}$, and $\Delta S^{\#}$ for 30NP, 50NP, and 70NP samples are 481. 42, 436. 88, 358.26 kJ mol^{-1}, 627.08, 581.14, 499.04 kJ mol^{-1}, and − 115.30, − 115.22, − 115.04 J mol^{-1} K^{-1}, respectively. The negative value of $\Delta S^{\#}$ implies that molecules are more tightly aligned in the active state owing to dipole–dipole interactions [57]. It is clear that the values of E, $\Delta H^{\#}$ and $\Delta G^{\#}$ decrease significantly with increasing of NP in the mixtures while the entropy $\Delta S^{\#}$ is almost constant at − 115 J mol^{-1} K^{-1} for all values of NP. This may be connected to the CaO content that favors the crystallization process.

Based on the exothermic form of the crystallization peak, the n Avrami coefficient can be calculated as follows [22, 57]:

$$n = \frac{2.5RT_c^2}{\Delta TE_c} \tag{12}$$

where ΔT is the crystallization peak's width at half maximum.

The morphology of the developing crystals can be predicted from the values of the Avrami constant [58]. The n exponent takes a steady state with a value of ~ 3.00 at low and medium phosphate content and reach a value of 4.10 after high NP addition, as listed in Table 3.

Matusita et al. [59, 60] given a model (Eq. 13) for determining out the m parameter, a numerical value that is dependent on the crystal growth's dimensions.

$$\ln\left(\frac{\beta^n}{T_c^2}\right) = -\frac{mE_c}{RT_c} + \text{constant} \tag{13}$$

where m is the numerical parameter and E_c is the crystallization activation energy. m = 1 indicates that surface

Table 2 Various crystallization kinetic characteristics exit for different samples

Sample		β\K min^{-1}				Average
		5	10	20	30	
30NP	E_{ck} (kJ mol^{-1})	491.77 ± 8.55				
	E_{cab1} (kJ mol^{-1})	498.84 ± 8.55				
	E_{cab2} (kJ mol^{-1})	502.16 ± 8.55				
	$\nu \times 10^{14}$ (s^{-1})	5.83				
	$k_0 \times 10^{14}$ (s^{-1})	5.60				
	$\Delta H^{\#}$ (kJ mol^{-1})	481.42	481.34	481.42	481.34	481.42 ± 8.55
	$\Delta G^{\#}$ (kJ mol^{-1})	624.67	625.78	624.67	625.78	624.67 ± 8.55
	$\Delta S^{\#}$ (J mol^{-1} K^{-1})	− 115.16	− 115.23	− 115.16	− 115.23	− 115.16 ± 8.55
50NP	E_{ck} (kJ mol^{-1})	447.29 ± 4.96				
	E_{cab1} (kJ mol^{-1})	453.94 ± 4.96				
	E_{cab2} (kJ mol^{-1})	457.27 ± 4.96				
	$\nu \times 10^{17}$ (s^{-1})	1.33				
	$k_0 \times 10^{17}$ (s^{-1})	1.27				
	$\Delta H^{\#}$ (kJ mol^{-1})	437.08	436.97	436.78	436.67	436.88 ± 4.96
	$\Delta G^{\#}$ (kJ mol^{-1})	578.37	579.82	582.42	583.95	581.14 ± 4.96
	$\Delta S^{\#}$ (J mol^{-1} K^{-1})	− 115.06	− 115.14	− 115.29	− 115.38	− 115.22 ± 4.96
70NP	E_{ck} (kJ mol^{-1})	368.22 ± 2.72				
	E_{cab1} (kJ mol^{-1})	375.21 ± 2.72				
	E_{cab2} (kJ mol^{-1})	378.45 ± 2.72				
	$\nu \times 10^{18}$(s^{-1})	1.45				
	$k_0 \times 10^{18}$ (s^{-1})	1.39				
	$\Delta H^{\#}$ (kJ mol^{-1})	358.26	358.12	358.26	358.12	358.26 ± 2.72
	$\Delta G^{\#}$ (kJ mol^{-1})	495.72	497.73	495.72	497.73	495.72 ± 2.72
	$\Delta S^{\#}$ (J mol^{-1} K^{-1})	− 114.84	− 114.96	− 114.84	− 114.96	− 114.84 ± 2.72

Table 3 Morphological parameters n and m obtained in the present study

Sample	Parameter	
	n	m
30NP	2.95	3.15
50NP	2.90	3.01
70NP	4.10	3.05

crystallization is prevalent, and m = 3 indicates that bulk crystallization is predominant (see Table 4) [61].

The plots of $\ln\left(\beta^n/T_c^2\right)$ vs. $10^3/T_c$ for mullite formation in kaolin-NP mixtures are shown in Fig. 8. The plots show straight lines and the m values (see Table 3) can be deduced from the slopes of plots. As seen from Table 3, it

Table 4 Different crystallization mechanisms [33, 72]

Crystallization mechanism	Avrami parameter\n	Numerical factor\m
Bulk crystallization with a constant number of nuclei (i.e. the number of nuclei is independent of the heating rate)		
Three-dimensional growth of crystals	3	3
Two-dimensional growth of crystals	2	2
One-dimensional growth of crystals	1	1
Bulk crystallization with an increasing number of nuclei (i.e. the number of nuclei is inversely proportional to the heating rate)		
Three-dimensional growth of crystals	4	3
Two-dimensional growth of crystals	3	2
One-dimensional growth of crystals	2	1
Surface crystallization	1	1

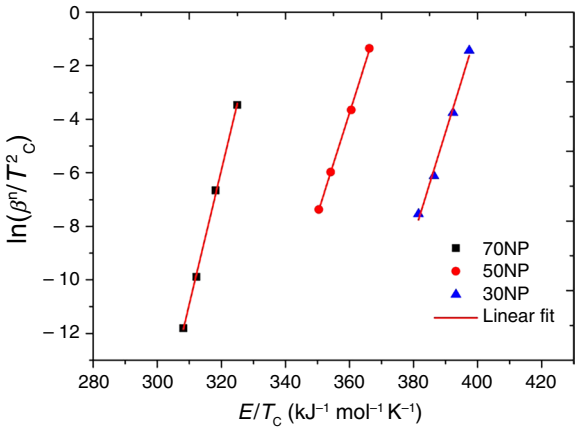

Fig. 8 Plots of Matusita-Kissinger for the compounds 30NP, 50NP, and 70NP

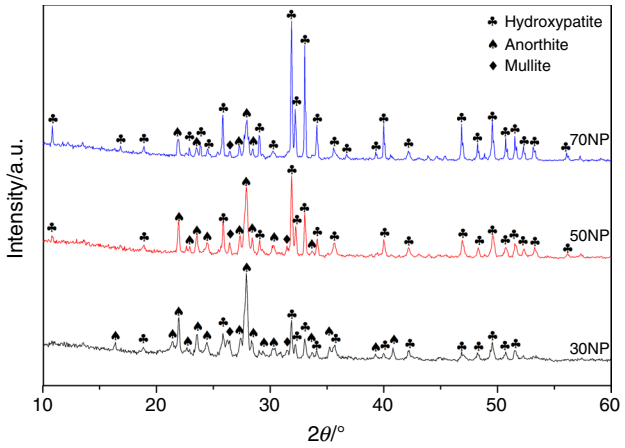

Fig. 9 XRD patterns of the samples sintered at 1473 K for 2 h

is found that for mullite formation, m is close to ~ 3.00 for all the samples. In the present study, bulk crystallization with a constant number of nuclei (n = m = 3) is controlled the mullite formation for low and medium NP concentrations. On the other hand, growing number of nuclei in bulk crystallization (n = 3 and m = n + 1) is the process mechanism for the sample containing high NP amount. This difference may be linked to the higher CaO amount in 70 NP sample that favors/improves the crystallization process. These results confirm that obtained in Fig. 5b, where the formation rate showed higher value for the 70 NP sample and differs from the other compounds, almost with steady dx/dt value.

It should be noted that while surface and bulk crystallization may occur concurrently during the DTA run, the samples' particle size has a significant impact on that process [36]. However, many controversial results show that bulk nucleation is the major process in mullite crystallization, with crystal development regulated by diffusion at a constant number of nuclei in kaolin. Therefore, the crystallization process depends of many factors including chemical composition, the crystal structure which crystallized the synthesized process, and others. It is also known that the contribution of bulk nucleation reduces as the heating rate increases [61].

X-ray diffraction spectra of 30, 50, and 70NP samples treated at 1473 K for 2 h, are presented in Fig. 9. Three phases are present in the samples' XRD spectra, which are Hydroxyapatite, anorthite, and mullite. It is clear that in the 30NP sample, the peaks of hydroxyapatite phase are observed with low intensity comparing with rest samples. On the other hand, as the NP amount increased from 50 to 70% the hydroxyapatite peaks intensity increased, which indicated the better crystallization. Meanwhile, the anorthite and mullite phase's peaks intensities decreased as the amount of NP in the combination increased. The anorthite formation is attributed to the reaction between kaolin and CaO, which obtained from calcite decomposition [47].

Figure 10 displays the microstructure of samples with varying NP concentrations that were sintered at 1473 K for two hours. When NP content was low, the microstructure is very heterogeneous, with large mullite grains found in the matrix. The grains corners are likewise rounded. These suggest the formation of a liquid phase, which is responsible for the uneven growth of mullite grains [62, 63]. Large grain growth might also be observed (Fig. 10a). It has been reported, when microstructural limitations are present, mullite grows in an equiaxed shape. However, with increasing NP content, they were made of nanometric (and agglomerated) hydroxyapatite grains with elongated forms [64]. Indeed, the microstructure of the samples shows a larger amount of pores and cracks (Fig. 10b, c). Additionally, it is evident that the pore's origin can be attributed to the gas produced by the dissolution reaction and the difficulties of sintering with the insertion of NP [65].

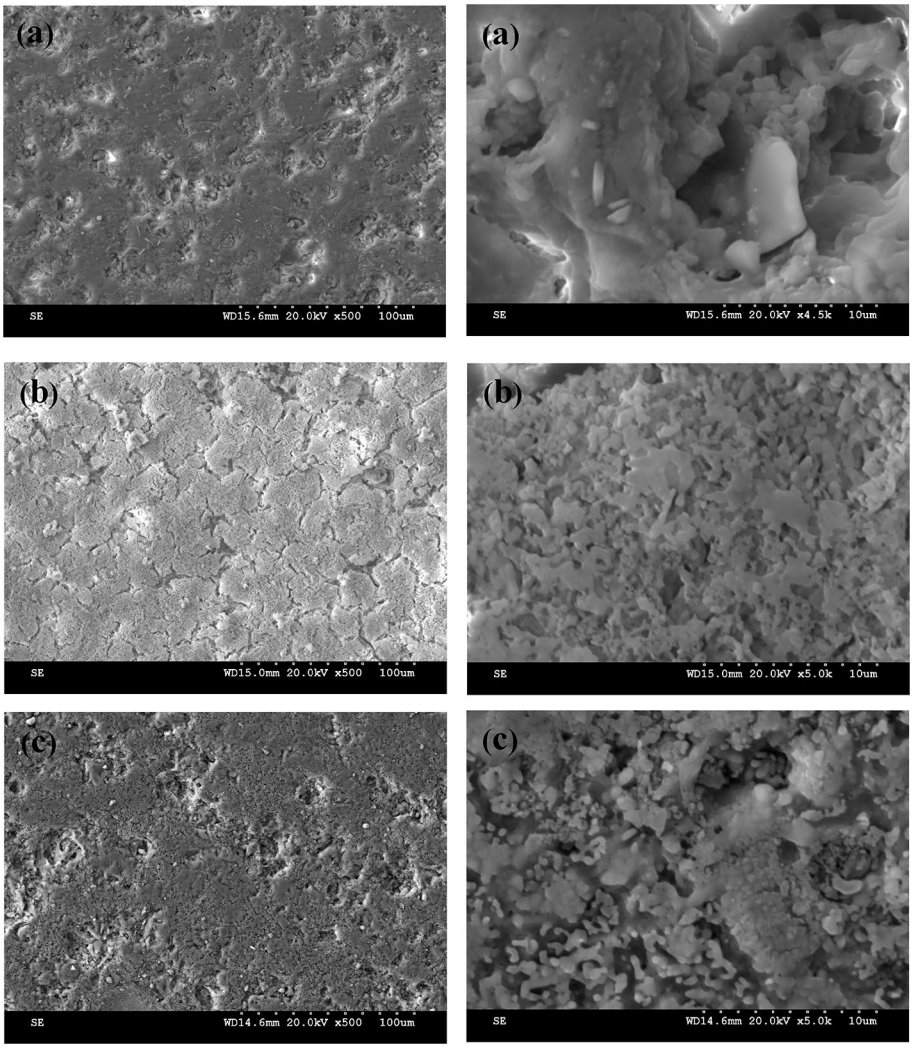

Fig. 10 SEM micrographs of the samples sintered at 1473 K for 2 h: **a** 30 NP, **b** 50 NP, and 70NP

Conclusions

The mullite phase crystallization kinetics synthetized from kaolin and natural phosphate materials was examined in non-isothermal environments. The main objective is to determine the associated kinetic parameters. The curves of differential thermal analysis reveal that there are multiple phase transitions during the heating process, including the mullite and hydroxyapatite crystal structures. The temperature of mullite crystallization was around ~ 1200 to 1300 K. Moreover, the thermodynamic parameters including enthalpy $\Delta H^{\#}$, energy of activation E_c, free enthalpy $\Delta G^{\#}$ and entropy $\Delta S^{\#}$, were calculated by several methods. The average value of $\Delta H^{\#}$ and $\Delta G^{\#}$ for 30 NP, 50 NP, and 70 NP mixtures are 481. 42, 436. 88, 358.26 and 627.08, 581.14, 499.04 kJ mol^{-1}, respectively. The entropy energy was around − 115.04 J mol^{-1} K^{-1} for all samples. The values of the growth morphological parameters n and m are determined for 30 NP and 50 NP samples, indicating a bulk nucleation with a fixed number of nuclei (n = m = 3), whereas, 70 NP compounds has followed the same process with varying number of nuclei (n = 3 and m = 4). Therefore, the CaO amount come from NP acts as structural modifier and favors the crystallization process of mullite phase. Finally, Algerian natural substances can be utilized for producing the mullite crystal structure at low costs.

Acknowledgements Mr. G. Moreau from the Laboratoire des Matériaux Céramiques et Procédés Associés, Université de Valenciennes et du Hainaut-Cambrésis, France, is acknowledged by the authors for his assistance with the SEM observations.

Funding No funding was received to assist with the preparation of this manuscript.

Declarations

Conflict of interest The authors declare no conflict of interest.

References

1. Schneider H, Schreuer J, Hildmann B. Structure and properties of mullite-a review. J Eur Ceram Soc. 2008;28:329–44.
2. Heraiz M, Sahnoune F, Hrairi M, Saheb N, Ouali A. Kinetics of mullite formation from kaolinite and boehmite. Mol Cryst Liq Cryst Lett. 2016;628:55–64.
3. Barrientos-Hernández FR, Pérez-Labra M, Lobo-Guerrero A, Reyes-Pérez M, Juárez-Tapia JC, Hernández-Ávila J, Cardoso-Legorreta E, Hernández-Lara JP. Effect of particle size and sintering temperature on the formation of mullite from Kyanite and Aluminum mixtures. Adv Mater Sci Eng. 2021;2021:6678297–310.
4. EL-Rafei AM, Mansour TS. Physico-mechanical and microstructure characteristics of porous mullite ceramics. SILICON. 2023;15:7157–70.
5. Bella ML, Hamidouche M, Gremillard L. Preparation of mullite-alumina composite by reaction sintering between Algerian kaolin and amorphous aluminum hydroxide. Ceram Int. 2021;47:16208–20.
6. Chen L, Wang Z, XueZ ZG, Wang S. Preparation of mullite ceramics with equiaxial grains from powders synthesized by the sol-gel method. Ceram Int. 2022;48:4754–62.
7. Sanad MMS, Rashad MM, Abdel-Aal EA, El-Shahat MF. Synthesis and characterization of nanocrystalline mullite powders at low annealing temperature using a new technique. J Eur Ceram Soc. 2012;16:4249–55.
8. Katsuki H, Furuta S, Komarneni S. Formation of novel ZSM-5/porous mullite composite from sintered kaolin honeycomb by hydrothermal reaction. J Am Ceram Soc. 2000;83:1093–7.
9. Chandran RG, Chandrashekar BK, Ganguly C, Patil KC. Sintering and microstructural investigations on combustion processed mullite. J Eur Ceram Soc. 1996;16:843–9.
10. Auger ML, Sarin VK. A kinetic investigation of CVD mullite coatings on Si-based ceramics. Int J Refract Met Hard Mater. 2001;19:479–94.
11. Ji H, MiX TQ, Liu C, Yao J, Ma S, Zeng G. Recycling of mullite from high-alumina coal fly ash by a mechanochemical activation method: Effect of particle size and mechanism research. Sci Total Environ. 2021;784:147–100.
12. Mebrek A, Rezzag H, Benayache S, Azzi A, Taibi Y, Ladjama S, Touati N, Bouchoucha S. Effect of chamotte on the structural and microstructural characteristics of mullite elaborated via reaction sintering of Algerian kaolin. J Mater Res Technol. 2019;8:4010–8.
13. Ren Q, Li H, Wu X, Huo Z, Hai O, Lin F. Effect of the calcining temperatures of low-grade bauxite on the mechanical property of mullite ceramics. Int J Appl Ceram Technol. 2018;15:554–62.
14. Raghdi A, Heraiz M, Sahnoune F, Saheb N. Mullite-zirconia composites prepared from halloysite reaction sintered with boehmite and zirconia. Appl Clay Sci. 2017;146:70–80.
15. Jing Y, Deng X, Li J, Bai C, Jiang W. Fabrication and properties of SiC/mullite composite porous ceramics. Ceram Int. 2014;40:1329–34.
16. Valášková M, Blahůšková V, Vlček J. Effects of kaolin additives in fly ash on sintering and properties of mullite ceramics. Minerals. 2021;11:887.
17. Jana A, Ray D. Synthesis and characterization of sol-gel derived monophasic mullite powder. Cerâmica. 2020;66:307–13.
18. Belhouchet H, Hamidouche M, Torrecillas R, Fantozzi G. The non-isothermal kinetics of mullite formation in boehmite–zircon mixtures. J Therm Anal Calorim. 2014;116:795–803.
19. Sahnoune F, Chegaar M, Saheb N, Goeuriot P, Valdivieso F. Differential thermal analysis of mullite formation from Algerian kaolin. Adv Appl Ceram. 2008;107:9–13.
20. Okada K. Activation energy of mullitization from various starting materials. J Eur Ceram Soc. 2008;28:377–82.
21. Tkalcec E, Ivankovic H, Nass R, Schmidt H. Crystallization kinetics of mullite formation in diphasic gels containing different alumina components. J Eur Ceram Soc. 2003;23:1465–75.
22. Romero M, Martín-Márquez J, Rincón JM. Kinetic of mullite formation from a porcelain stoneware body for tiles production. J Eur Ceram Soc. 2006;26:1647–52.
23. Francis A, Vilminot S. Crystallisation kinetics of mullite glass-ceramics obtained from alumina–silica wastes. Int J Sustainable Eng. 2013;6:74–81.
24. Flores-Vélez LM, Lomelí M, Sánchez G, Domínguez O. Mullitization kinetics from kaolinite incorporating nanometric Ba and Ca fluorides. Ceram Int. 2015;41:7903–9.
25. Li DX, Thomson WJ. Kinetic mechanisms for mullite formation from sol-gel precursors. J Mater Res. 1990;5:1963–9.
26. Vieira SC, Ramos AS, Vieira MT. Mullitization kinetics from silica-and alumina-rich wastes. Ceram Int. 2007;33:59–66.
27. Pooladvand H, Baghshahi S, Mirhadi B, Souri AR, Arabi H. Effect of MgO and CaO on transformation of andalusite to mullite. J Mater Eng Perform. 2012;21:1637–44.
28. Qiankun G, Xuekun T, Hongsen W, Jiaxin S, Deze O, Fei Z, Xinhong L. Effect of CaO impurity on mullite formation from SiO_2 Gel and Al_2O_3 powders. China's Refractories. 2024;33:34.
29. Sahraoui T, Chouia F, Bourezg YI, Guelil A. Effect of natural phosphate content on the growth kinetics of hydroxyapatite crystals grown from kaolin clay. Mater Chem Phys. 2022;292: 126865.
30. Belhouchet H, Chouia F, Hamidouche M, Leriche A. Preparation and characterization of anorthite and hydroxyapatite from Algerian kaolin and natural phosphate. J Therm Anal Calorim. 2016;126:1045–57.
31. Sahnoune F, Chegaar M, Saheb N, Goeuriot P, Valdivieso F. Algerian kaolinite used for mullite formation. Appl Clay Sci. 2008;38:304–10.
32. Ouali A, Sahnoune F, Heraiz M, Belhouchet H. Sinterability and thermal properties of cordierite ceramics prepared from Algerian kaolinite and magnesium hydroxide. Mol Cryst Liq Cryst. 2016;628:65–71.
33. Raynaud S, Champion E, Bernache-Assollant D, Thomas P. Calcium phosphate apatites with variable Ca/P atomic ratio I. Synthesis, characterization and thermal stability of powders. Biomaterials. 2002;23:1065–72.
34. Graba Z, Hamoudi S, Bekka D, Bezzi N, Boukherroub R. Influence of adsorption parameters of basic red dye 46 by the rough and treated Algerian natural phosphates. J Ind Eng Chem. 2015;25:229–38.
35. Koumoulidis GC, Katsoulidis AP, Ladavos AK, Pomonis PJ, Trapalis CC, Sdoukos AT, Vaimakis TC. Preparation of hydroxyapatite via microemulsion route. J Colloid Interface Sci. 2003;259:254–60.
36. Chen YF, Wang MC, Hon MH. Phase transformation and growth of mullite in kaolin ceramics. J Eur Ceram Soc. 2004;24:2389–97.
37. Gao X, Zhang D, Feng X, Zhang J, Yuqing P, Zhicheng P, Zongming D. Effect of particle size of associated rare earth kaolin powder on the sintering and properties of synthetic mullite. J Am Ceram Soc. 2024;107:2658–67.
38. Rouabhia F, Nemamcha A, Moumeni H. Elaboration and characterization of mullite-anorthite-albite porous ceramics prepared from Algerian kaolin. Cerâmica. 2018;64:126–32.
39. Sadli N, May A, Hamidouche M, Henniche A, Belhouchet H, Boudouh H. Investigations on kaolin mixtures: Impact on mullite formation kinetics and microstructure evolution. Int J Appl Ceram Technol. 2024;21:3950–66.
40. Ptáček P, Křečková M, Šoukal F, Opravil T, Havlica J, Brandštetr J. The kinetics and mechanism of kaolin powder sintering I. The

dilatometric CRH study of sinter-crystallization of mullite and cristobalite. Powder Technol. 2012;232:24–304.
41. Chen YF, Wang MC, Hon MH. Transformation kinetics for mullite in kaolin–Al_2O_3 ceramics. J Mater Res. 2003;18:1355–62.
42. Ji H, Fang M, Huang Z, Chen K, Xu Y, Liu Y, Huang J. Effect of La_2O_3 additives on the strength and microstructure of mullite ceramics obtained from coal gangue and γ-Al_2O_3. Ceram Int. 2013;39:6841–6.
43. Rodrigues AM, Narváez-Semanate JL, Cabral AA, Rodrigues ACM. Determination of crystallization kinetics parameters of a $Li_{1,5}$ $Al_{0,5}$ $Ge_{1,5}$ $(PO_4)_3$ (LAGP) glass by differential scanning calorimetry. Mater Res. 2013;16:811–6.
44. Campos AL, Silva NT, Melo FCL, Oliveira MAS, Thim GP. Crystallization kinetics of orthorhombic mullite from diphasic gels. J Non-Cryst Solids. 2002;304:19–24.
45. Khaldi M, Bourezg YI, Kharroubi M, Sahnoune F, Harfouche M, Keziz A, Maacha M, Gacem L, Bradai D. Effect of copper oxide amount on non-isothermal crystallization kinetics of diphosphate glasses. J Non-Cryst Solids. 2024;630: 122904.
46. Qin M, Tian Y, Hao H, Li G, Zhou Y, Bai P. Effects of $CaCO_3$ additive on properties and microstructure of corundum-and mullite-based ceramic proppants. Int J Appl Ceram Technol. 2020;17:1026–32.
47. Kłosek-Wawrzyn E, Małolepszy J, Murzyn P. Sintering behavior of kaolin with calcite. Procedia Eng. 2013;57:572–82.
48. Kissinger HE. Reaction kinetics in differential thermal analysis. Anal Chem. 1957;29:1702–6.
49. Kissinger HE. Variation of peak temperature with heating rate in differential thermal analysis. J Res Natl Bur Stand. 1956;57:217–21.
50. Ptáček P, Opravil T, Šoukal F. Introduction of novel kinetic approach to calculation of activation energy and its application to the sinter-crystallization of strontian feldspar. Ceram Int. 2016;42:16969–80.
51. Augis JA, Bennett JE. Calculation of the Avrami parameters for heterogeneous solid state reactions using a modification of the Kissinger method. J Therm Anal. 1978;13:283–92.
52. Yinnon H, Uhlmann DR. Applications of thermoanalytical techniques to the study of crystallization kinetics in glass-forming liquids, part I: theory. J Non-Cryst Solids. 1983;54:253–75.
53. Ondro T, Al-Shantir O, Csáki Š, Lukáč F, Trník A. Kinetic analysis of sinter-crystallization of mullite and cristobalite from kaolinite. Thermochim Acta. 2019;678:178312–8.
54. Elmas E, Yildiz K, Toplan N, Toplan HÖ. The non-isothermal kinetics of mullite formation in mechanically activated kaolinite–alumina ceramic system. J Therm Anal Calorim. 2012;108:1201–6.
55. Silva RA, Teixeira SR, Souza AE, Santos DI, Romero M, Rincón JM. Nucleation kinetics of crystalline phases from a kaolinitic body used in the processing of red ceramics. Appl Clay Sci. 2011;52:165–70.
56. Pourmortazavi SM, Kohsari I, Teimouri MB, Hajimirsadeghi SS. Thermal behaviour kinetic study of dihydroglyoxime and dichloroglyoxime. Mater Lett. 2007;61:4670–3.
57. Danewalia SS, Singh K, Arya SK. Influence of vanadium oxide on non-isothermal crystallization kinetics of zinc lithium borate glasses. J Non-Cryst Solids. 2021;553:120471–9.
58. Johnson BR, Kriven WM, Schneider J. Crystal structure development during devitrification of quenched mullite. J Eur Ceram Soc. 2001;21:2541–62.
59. Matusita K, Sakka S, Matsui Y. Determination of the activation energy for crystal growth by differential thermal analysis. J Mater Sci. 1975;10:961–6.
60. Matusita K, Sakka S. Kinetic study of the crystallisation of glass by differential scanning calorimetry. Phys Chem Glasses. 1979;20:81–4.
61. Erol M, Küçükbayrak S, Ersoy-Meriçboyu A, Öveçoğlu ML. Crystallization behaviour of glasses produced from fly ash. J Eur Ceram Soc. 2001;21:2835–41.
62. Tripathi HS, Ghosh A, Halder MK, Mukherjee B, Maiti HS. Microstructure and properties of sintered mullite developed from Indian bauxite. Bull Mater Sci. 2012;35:639–43.
63. Sarkar R, Mallick M. Formation and densification of mullite through solid-oxide reaction technique using commercial-grade raw materials. Bull Mater Sci. 2018;41:1–8.
64. Guo X, Yan H, Zhao S, Li Z, Li Y, Liang X. Effect of calcining temperature on particle size of hydroxyapatite synthesized by solid-state reaction at room temperature. Adv Powder Technol. 2013;24:1034–8.
65. Zhao X, Liu Q, Yang J, Zhang W, Wang Y. Sintering behavior and mechanical properties of mullite fibers/hydroxyapatite ceramic. Materials. 2018;11:1859.